Silicon Quantum Dot Nanoparticles with Antifouling Coatings for Immunostaining on Live Cancer Cells

Chang-Ching Tu,[†,‡] Kuang-Po Chen,[†] Tsu-An Yang,[†] Min-Yuan Chou,[§] Lih Y. Lin,[∥] and Yaw-Kuen Li[*,†]

[†]Department of Applied Chemistry, National Chiao Tung University, Hsinchu, Taiwan 300, ROC

[‡]LumiSands Inc., Seattle, Washington 98105, United States

[§]Biomedical Technology and Device Research Laboratories, Industrial Technology Research Institute, Hsinchu, Taiwan 310, ROC

[∥]Department of Electrical Engineering, University of Washington, Seattle, Washington 98195, United States

Ⓢ *Supporting Information*

ABSTRACT: Fluorescent silicon quantum dots (SiQDs) have shown a great potential as antiphotobleaching, nontoxic and biodegradable labels for various in vitro and in vivo applications. However, fabricating SiQDs with high water-solubility and high photoluminescence quantum yield (PLQY) remains a challenge. Furthermore, for targeted imaging, their surface chemistry has to be capable of conjugating to antibodies, as well as sufficiently antifouling. Herein, antibody-conjugated SiQD nanoparticles (SiQD-NPs) with antifouling coatings composed of bovine serum albumin (BSA) and polyethylene glycol (PEG) are demonstrated for immunostaining on live cancer cells. The monodisperse SiQD-NPs of diameter about 130 nm are synthesized by a novel top-down method, including electrochemical etching, photochemical hydrosilylation, high energy ball milling, and "selective-etching" in HNO_3 and HF. Subsequently, the BSA and PEG are covalently grafted on to the SiQD-NP surface through presynthesized chemical linkers, resulting in a stable, hydrophilic, and antifouling organic capping layer with isothiocyanates as the terminal functional groups for facile conjugation to the antibodies. The in vitro cell viability assay reveals that the BSA-coated SiQD-NPs had exceptional biocompatibility, with minimal cytotoxicity at concentration up to 1600 $\mu g\ mL^{-1}$. Under 365 nm excitation, the SiQD-NP colloid emits bright reddish photoluminescence with PLQY = 45−55% in organic solvent and 5−10% in aqueous buffer. Finally, through confocal fluorescent imaging and flow cytometry analysis, the anti-HER2 conjugated SiQD-NPs show obvious specific binding to the HER2-overexpressing SKOV3 cells and negligible nonspecific binding to the HER2-nonexpressing CHO cells. Under similar experimental conditions, the immunofluorescence results obtained with the SiQD-NPs are comparable to those using conventional fluorescein isothiocyanate (FITC).

KEYWORDS: silicon quantum dots, photoluminescence, antifouling coatings, bioconjugation, biological labels, immunofluorescence
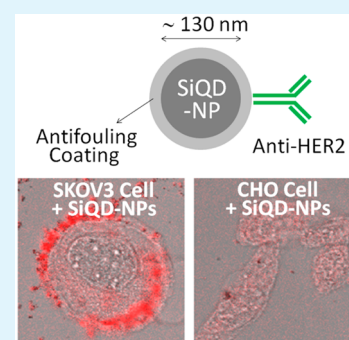
1. INTRODUCTION

Optical fluorescence has become an essential tool in nowadays biomedical research, from in vitro cellular imaging, to in vivo visualization of living animals for preclinical research, to sensing and diagnosis.[1−3] For clinical applications, although fluorescence light cannot penetrate as deeply as other physical means, such as magnetic resonance, X-ray or ultrasound, lately fluorescent "tumor paint" has emerged as an intraoperative visualization agent for precise surgical removal of cancerous tissues.[4] Over the past decades, organic dyes as well as fluorescent proteins or peptides have been the most widely used biomedical fluorophores. However, they are susceptible to photobleaching which may cause significant reliability concern especially for long-term or time-lapse imaging applications.[5] Furthermore, the photobleaching issue becomes even more severe for those dyes emitting in red or IR, which are wavelengths desirable for deep tissue imaging.[6] Recently, inorganic semiconductor nanocrystals or quantum dots (QDs) have emerged as a promising substitute of those organic chromophores for better photochemical stability. In addition to antiphotobleaching, the semiconductor QDs possess several other optical properties beneficial for biomedical imaging, such as size-dependent photoluminescence (PL), high photoluminescence quantum yield (PLQY), narrow emission line width, broad excitation spectrum, and large Stokes shift. Immunofluorescence based on the QDs has been demonstrated in various in vitro and in vivo studies.[7−10] However, until now, the most commonly used QDs in biomedical research are still composed of either II−VI (e.g., CdSe) or III−V (e.g., InP) compound semiconductors, all of which contain heavy metals even if they are cadmium-free (e.g., $InAs_xP_{1−x}$/InP/ZnSe, CuInS/ZnS).[11,12] Although capping with multiple shells and biocompatible coatings may prevent the leakage of heavy-metals and alleviate acute cytotoxicity, the long-term clearance of QD constituents in vivo is still unclear,[13] diminishing their potential to be considered for clinical usage.
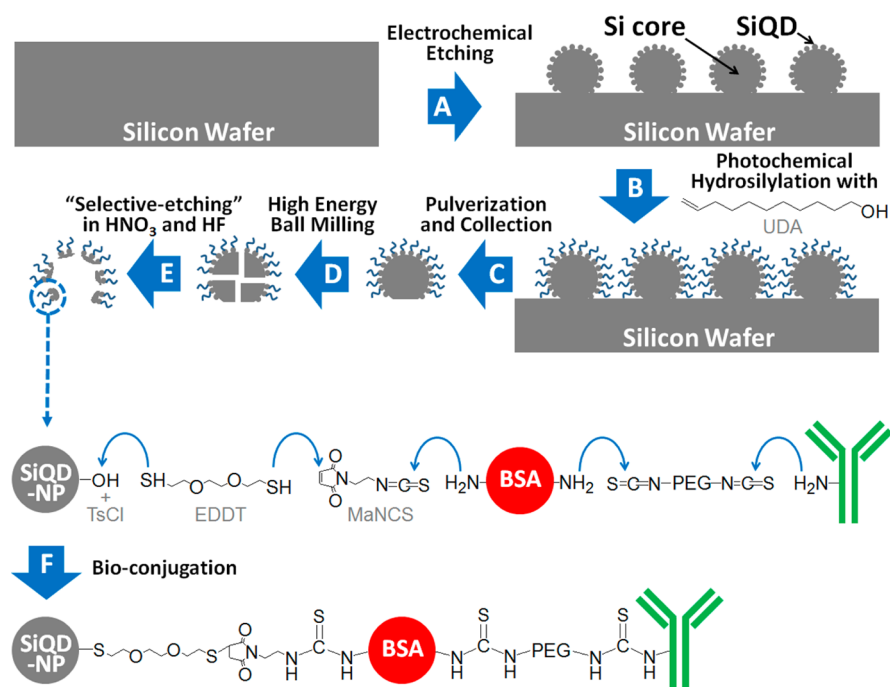
Figure 1. Key steps to fabricate the hydroxyl-terminated SiQD-NPs, including (A) electrochemical etching on a silicon wafer, (B) photochemical hydrosilylation with UDA on the SiQDs, (C) mechanical pulverization and collection from the silicon wafer surface, (D) HEBM, and (E) selective-etching in HNO₃ and HF. (F) For the bioconjugation, short chemical linkers, EDDT and MaNCS, were used to anchor BSA on top of the hydroxyl-terminated SiQD-NPs, and bifunctional polymers, isothiocyanate−PEG−isothiocyanate, were used to connect the surface-immobilized BSA with the antibodies.

Photoluminescent silicon quantum dots (SiQDs) can avoid the photobleaching issue of organic dyes,[14−16] at the same time not containing the heavy-metal-toxicity of cadmium-based QDs. In a recent biocompatibility study, the in vitro inhibitory particle concentration corresponding to 50% cell viability (IC_{50}) was determined to be >500 $\mu g\ mL^{-1}$ for SiQDs, compared with only 10 to 20 $\mu g\ mL^{-1}$ for cadmium-based QDs.[17] In addition, a tolerable dosage of SiQDs in vivo was estimated to be 60 nmol per mouse,[17] which is about 10 times higher than the maximum dosage of CdSe-ZnS core−shell QDs used for in vivo tumor imaging.[10] For the biodistribution studies of SiQDs post intravenous administration, although immediate uptake in mononuclear phagocyte system (MPS) organs, such as liver and spleen, has been observed, the accumulated SiQDs underwent gradual degradation into excretable silicic acid and was completely cleared from the body in 4 to 8 weeks.[17,18] Such biodegradability contrasts with the slow clearance of cadmium-based QDs, for which most of the cadmium constituents remained in the liver, spleen and kidney even after 90 days.[13]

In addition to the toxicology studies, the efficacy studies of SiQDs as fluorescent biological labels have been reported.[19] Notably, Park et al. used dextran-coated porous silicon nanoparticles for in vivo imaging on tumors, within which the nanoparticles were just passively accumulated due to the enhanced permeability and retention (EPR) effect,[18] rather than through antibody−antigen specific binding which has better specificity and selectivity. Erogbogbo et al. demonstrated SiQDs encapsulated in phospholipid micelles for cellular imaging, tumor vasculature targeting, and sentinel lymph node mapping in live mice.[17,20] However, in their works, the micelles may become unstable when the concentration of phospholipids is below its critical micelle concentration (CMC)

and the carboxylates activated by 1-Ethyl-3-(3-(dimethylamino)propyl)carbodiimide (EDC) are susceptible to hydrolysis which may cause the bioconjugation process inconsistent. Herein, we demonstrate highly photoluminescent, water-dispersible silicon quantum dot nanoparticles (SiQD-NPs) with antifouling coatings composed of bovine serum albumin (BSA) at the inner layer and polyethylene glycol (PEG) at the outer layer. Particularly, the BSA is an exceptionally hydrophilic plasma protein and has been widely used to block nonspecific binding sites in various biological applications. Furthermore, the outmost surface of the SiQD-NPs is terminated with isothiocyanate (−N═C═S), which is resistant to hydrolysis and can easily react with the primary amines of the antibodies. Most importantly, all the organic capping elements are covalently bonded to the SiQD-NP surface through presynthesized chemical linkers, resulting in more reliable surface chemistry than the conventional micelle formation method.

Since the demonstration of visible PL emitted from porous silicon in 1990s,[21] numerous techniques have been developed to fabricate SiQDs, and depending on the physical size of the starting materials, they can be categorized into two types, "bottom-up" and "top-down". The bottom-up methods involve the nucleation of precursor molecules in gas- or solution-phase upon energy input, such as laser- or plasma-assisted aerosol decomposition of silane gas (SiH_4),[22,23] thermally degrading Si precursors with high pressure,[24] thermal processing of sol−gel polymers derived from $HSiCl_3$,[25] and solution-based reduction of $SiCl_4$.[26] The aforementioned methods can usually produce free-standing SiQDs of size only a few nanometers in diameter. However, for in vivo imaging, such small silicon nanocrystals (<5.5 nm) will be rapidly cleared from the bloodstream through renal filtration and urinary excretion before carrying
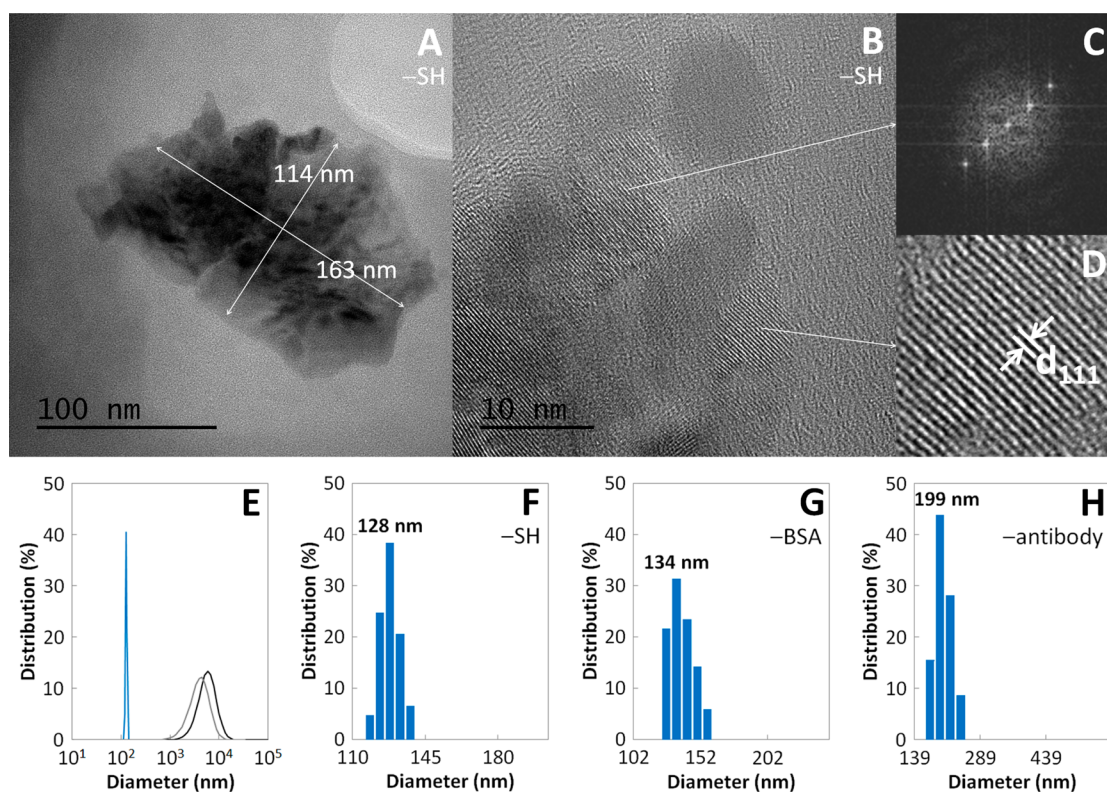
Figure 2. (A) TEM image of a thiol-terminated SiQD-NP. (B) HRTEM image of the porous silicon layer on the SiQD-NP surface, where clusters of spherelike SiQDs of diameter about 5 to 8 nm were observed. (C) FFT electron diffraction pattern of the marked SiQD in the middle. (D) Direct measurement of lattice spacing on the other marked SiQD, showing the same d_{111} value (3.14 Å) as calculated from the diffraction pattern in C. (E) Particle size distributions of the silicon powders just harvested from the silicon wafer (the black line), applied with the selective-etching step alone (the gray line) and applied with both the HEBM and selective-etching steps (the blue line). (F−H) Particle size distributions of the SiQD-NPs terminated with −SH, −BSA, and −antibody, respectively.

out their function.[27] Furthermore, the nanotoxicity in biological systems which is associated with the extremely small size (<100 nm) of nanomaterials has been reported.[28] On the other hand, the top-down methods, such as electrochemical etching on a crystalline silicon wafer, can fabricate fluorescent silicon nanoparticles of size ranging from 100 to 200 nm, which has been demonstrated suitable for both in vitro and in vivo imaging applications without the concerns of rapid renal excretion and nanotoxicity.[18] However, the crude product from the conventional electrochemical etching method is generally a mixture of bulk silicon pieces, with photoluminescent SiQDs attached on their surfaces. Therefore, typical mechanical methods such as sonication and filtration are often applied to extract the SiQDs and remove the larger silicon pieces, which inevitably leads to extremely low production yield and modest PLQY. In this work, we present a novel top-down method, including electrochemical etching, photochemical hydrosilylation, high energy ball milling (HEBM), and "selective-etching" in HNO₃ and HF, to produce SiQD-NPs of high colloidal stability, high PLQY (45−55% in organic solvent and 5−10% in aqueous buffer), and narrow size distribution (about 130 nm in diameter). Moreover, the overall synthesis process is ambient-compatible, efficient and potentially scalable.

2. RESULTS AND DISCUSSION

2.1. Synthesis of the SiQD-NPs. The fabrication process of the hydroxyl-terminated SiQD-NPs and the surface chemistry for conjugating to the antibodies is illustrated in Figure 1. First, a 6 in. p-type silicon wafer was electrochemically

etched at a constant current in an electrolyte comprising hydrofluoric acid and methanol, creating a red-fluorescing porous silicon layer on top (Figure S1A, B), in which microsize Si cores (Figure S2A) were covered with clusters of nanosize SiQDs (Figure S2B).[29] After treated with diluted hydrofluoric acid which renders silicon hydride (Si−H) passivation, the porous silicon layer was immersed in neat 10-Undecen-1-ol (UDA) under an oxygen-free condition. Subsequently, upon illumination with white light, a photochemical hydrosilylation reaction occurred, during which the unsaturated double bonds of UDA formed covalent bonds with the silicon hydrides, resulting in silicon carbide (Si−C) passivation. After hydrosilylation, the PL of the porous silicon layer became stronger and more uniform (Figure S1C, D). Noteworthily, the mechanism of the white light-induced hydrosilylation here is associated with the photoexcited excitons trapped on the SiQD surface.[30] Therefore, the silicon carbide passivation resides only on the SiQDs, leaving the rest porous silicon surfaces exposed for oxidation. Then, the porous silicon layer was mechanically pulverized and collected from the silicon wafer surface. The resulting fluorescent silicon powders (Figure S2C) were dispersed in isopropanol, followed by treating with HEBM for crumbling the microsized Si cores into small pieces. After HEBM, the colloid was selectively etched by an aqueous etchant composed of HNO₃ and HF, during which the nonradiative bulk silicon residues capped with silicon oxide were etched away, whereas the photoluminescent SiQDs with the silicon carbide passivation were mostly preserved. Until this step, the SiQD-NPs of much reduced sizes were produced

(Figure S2D), and their outmost surfaces were uniformly terminated hydroxyl groups, some from the hydroxyl ends of UDA bonded on the SiQDs and the other from the silicon oxide capped on the bare silicon surfaces. For the following bioconjugation, short chemical linkers, 2,2′-(Ethylenedioxy)-diethanethiol (EDDT) and 1-(2-Isothiocyanatoethyl)-1H-pyrrole-2,5-dione (MaNCS), were used to anchor BSA on the hydroxyl-terminated SiQD-NPs whose surfaces were preactivated by reacting with p-Toluenesulfonyl chloride (TsCl). Finally, bifunctional polymers, isothiocyanate−PEG−isothiocyanate with weight-average molecular weight (M_w = 3350, were used to connect the surface-immobilized BSA with the antibodies.

2.2. Structural Characterizations of the SiQD-NPs. In this section, the structures of the thiol-terminated the SiQD-NPs were further characterized by high resolution transmission electron microscope (HRTEM) and the overall particle sizes of the SiQD-NPs with different surface chemistry were measured by dynamic light scattering (DLS) methods. Figure 2A exhibits a typical thiol-terminated SiQD-NP featuring highly porous surfaces and an asymmetrical geometric shape. Zooming in on the porous silicon layer, irregular matrix structures comprising clusters of spherelike SiQDs of diameter about 5 to 8 nm were observed (Figure 2B). The SiQD sizes observed here are slightly larger than the previous result also obtained from a red-fluorescing porous silicon,[31] likely due to the additional silicon oxide shell resulting from the HNO_3 oxidation. Moreover, the FFT electron diffraction pattern of the marked SiQD in the middle (Figure 2C) can be indexed with space group $Fd3m$ and lattice spacing (d_{111}) 3.14 Å, both of which are characteristics of silicon. By direct measurement of the lattice spacing on the other marked SiQD (Figure 2D), the same d_{111} value was obtained. In summary, both observations unambiguously confirmed the attached SiQDs are crystalline, which is a critical factor contributing to the high PLQY of the SiQD-NPs.

As elucidated in Figure 1, the size of the Si core which mostly determines the overall particle size was greatly reduced by the steps of HEBM and selective-etching. For silicon powders just harvested from the silicon wafer (the step C in Figure 1), their particle sizes were in micrometers and with a wide distribution ranging from 1 to 10 μm (the black line in Figure 2E). If the selective-etching step alone was applied, the resulting particles became slightly smaller with majority sizes still above 1 μm (the gray line in Figure 2E). But when both the HEBM and selective-etching steps were employed (the step E in Figure 1), the overall particle sizes drastically shrank down to about 130 nm and became relatively monodisperse (the blue line in Figure 2E). During the bioconjugation process, the SiQD-NP surface chemistry changed sequentially from hydroxyl-, to thiol-, to BSA-, to antibody-terminated, so did the hydrodynamic sizes of the SiQD-NPs increase step by step (Figure 2F−H). The thiol-terminated SiQD-NPs had a narrow dispersion of hydrodynamic diameters centered at 128 nm, which is about the size shown in the TEM image (Figure 2A). The BSA has molecular weight (M_W) = 66.5 kDa and a hydrodynamic structure equivalent to a prolate ellipsoid of size about 14 nm × 4 nm × 4 nm.[32] Therefore, it is reasonable to obtain about 6 nm diameter increment from Figure 2F to G. On the other hand, given that the typical dimensions of immunoglobulin G (IgG, M_W = 150 kDa) are about 14.5 nm × 8.5 nm × 4.0 nm and the hydrodynamic diameter of the PEG here (M_W = 3350) is estimated to be only 1 nm,[33,34] about 65 nm diameter increment from Figure 2G to H suggests that antibody

agglomerations, such as dimmer formation, may occur on the SiQD-NP surfaces.[35]

2.3. Surface Chemistry of the SiQD-NPs. The spectra of attenuated total reflectance Fourier transform infrared spectroscopy (ATR-FTIR) of the SiQD-NPs with different surface chemistry are shown in Figure 3. The highlighted areas from
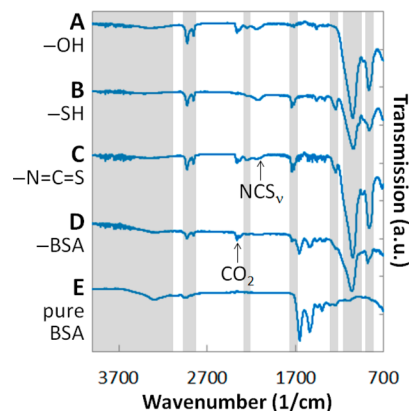

Figure 3. ATR-FTIR spectra of the SiQD-NPs terminated with (A) −OH, (B) −SH, (C) −N=C=S, and (D) −BSA, respectively. (E) An ATR-FTIR spectrum of pure BSA powders. The highlighted areas from left to right represent OH_{ν} (2400 to 3600 cm^{-1}), CH_{ν} (2925 and 2855 cm^{-1}), O−SiH_{ν} (2245 cm^{-1}), C=O_{ν} (1700 cm^{-1}), C−O_{ν} (1240 cm^{-1}), Si−O−Si_{ν} (950 to 1250 cm^{-1}), and O−SiH_{δ} (870 cm^{-1}). The absorption at 2360 cm^{-1} is due to the CO_2 in ambient air (ν, stretching; δ, deformation).

left to right represent the absorptions of OH_{ν} (2400 to 3600 cm^{-1}), CH_{ν} (2925 and 2855 cm^{-1}), O−SiH_{ν} (2245 cm^{-1}), C=O_{ν} (1700 cm^{-1}), C−O_{ν} (1240 cm^{-1}), Si−O−Si_{ν} (950 to 1250 cm^{-1}), and O−SiH_{δ} (870 cm^{-1}). After the steps of hydrosilylation, HEBM, and selective-etching, the outmost surfaces of the SiQD-NPs were homogeneously terminated with hydroxyl groups (Figure 3A), causing the broadband OH_{ν} absorption. Also in the spectrum, the strong CH_{ν} absorption is attributed to the 11-carbon alkyl chain of UDA, and the absorptions of O−SiH_{ν}, Si−O−Si_{ν} and O−SiH_{δ} belong to the characteristic IR features of oxidized SiQDs.[36] Then, the hydroxyl group was activated by TsCl, becoming −OTs which is a good leaving group for the nucleophilic attack by either one of the thiol (−SH) ends of EDDT. After the substitution reaction was complete (Figure 3B), the C−O_{ν} absorption due to the ethylenedioxy of EDDT appeared and the OH_{ν} absorption diminished accordingly. Additionally, the C=O_{ν} absorption here became more obvious likely because some of the hydroxyl groups of UDA got oxidized into carboxylic acids during the prolonged sonication in TsCl solution. Thereafter, the maleimide end of the short bifunctional linker, MaNCS, reacted with the remaining thiol end of EDDT, with the opposite isothiocyanate end exposed outward for the following conjugation with the BSA. The IR spectrum at this step (Figure 3C) is almost identical to the previous step, except the weak NCS_{ν} absorption (2110 cm^{-1}) emerged. Finally, the BSA, which consist of 59 lysine residues and 30 to 35 primary amines per molecule on the exterior available for reaction, were anchored on the SiQD-NP surfaces through isothiocyanate-amine coupling. The resulting IR spectrum (Figure 3D) is simply a superimposition of the pure BSA spectrum (Figure 3E) over the NCS-terminated spectrum (Figure 3C), indicating the BSA was successfully grafted onto the SiQD-NP surfaces.
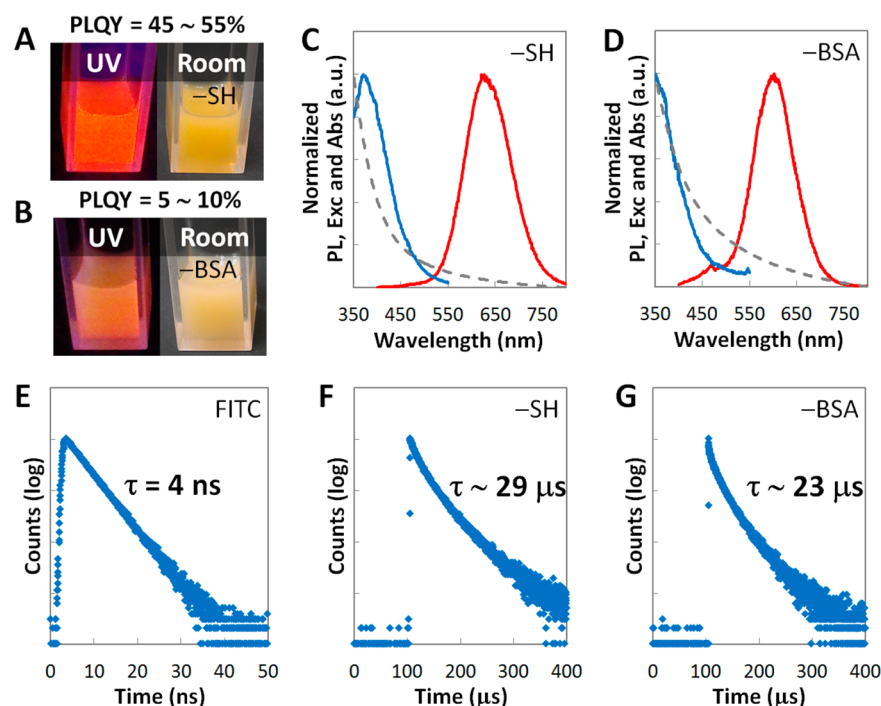
Figure 4. (A, B) Photographs and PLQY values of the suspensions of the SiQD-NPs terminated with −SH in THF and −BSA in 0.1 M pH 6 PB, respectively. (C, D) Normalized photoluminescence (PL, the red solid line), excitation (Exc, the blue solid line), and absorbance (Abs, the gray dash line) spectra of the suspensions of the SiQD-NPs terminated with −SH and −BSA, respectively. (E−G) PL lifetimes of FITC and thiol- and BSA-terminated SiQD-NPs, respectively.

2.4. Optical Characterizations of the SiQD-NPs.

The thiol-terminated SiQD-NPs can form a uniform suspension in tetrahydrofuran (THF). The resulting colloid looked clear and yellowish under room light and emitted bright reddish PL with PLQY = 45−55% under 365 nm excitation (Figure 4A). In spectral analysis, the colloid showed almost symmetric PL spectrum with a single peak at 621 nm and a full width at half-maximum (fwhm) = 114 nm, and the efficient excitation wavelengths ranged from 350 to 410 nm (Figure 4C). The absorbance spectrum here takes into account scattering and absorption by the Si cores and its trend of higher absorption in the shorter wavelengths resembles to other types of semiconductor nanocrystals in general. In comparison, after coated with the BSA, the SiQD-NPs became exceptionally water-dispersible and able to maintain prolonged uniform suspension in 0.1 M potassium phosphate buffer (PB) with pH 6. The translucent colloid looked pale yellowish under room light but the PLQY was quenched to 5−10% under 365 nm excitation (Figure 4B). Besides, the PL peak wavelength was blue-shifted to 602 nm, the fwhm decreased to 101 nm, and the efficient excitation range dwindled to from 350 to 385 nm (Figure 4D). The relatively broadband absorbance spectrum here as well as the colloid's nearly whitish color suggests that the SiQD-NP scattering in water was greatly enhanced by the BSA coating. Further modification by the isothiocyanate−PEG−isothiocyanate and conjugation to the antibodies did not change the optical properties of the BSA-terminated SiQD-NPs. The colloidal stability of both the thiol- and BSA-terminated SiQD-NPs was well enough to keep homogeneous and optically transparent suspension at 4 °C for 24 h. After 72 h, although slight sedimentation might occur, its original uniformity can be easily restored by short vortex agitation. The quenching of PLQY after the suspension medium changed from organic to aqueous solvents was also found in our previous study,[37] and it is likely associated with the absorption of polar molecules, such as water and dimethyl sulfoxide, on the SiQD surfaces. Through Coulomb interactions, the absorbed polar molecules stabilize the electrons or holes trapped at the oxide-related surface defect states and enhance nonradiative recombination processes.[38] On the other hand, silicon nanoparticles synthesized by the microwave-assisted nucleation methods have shown almost no alteration of optical properties after conjugated to proteins, as a result of their unique ligand protection system.[15,16] Therefore, in a similar way, the PLQY of the BSA-terminated SiQD-NPs here can be further improved by insulating the SiQDs from the PL-quenching molecules by coating with polymers or oxide shells. It is also noteworthy that the yellowish color of the SiQD-NP suspension and its relatively broadband absorbance spectrum were mainly attributed to the absorption of the Si cores, even if their sizes had been significantly reduced to about 130 nm. On top of that, photoexcitation inside the Si cores cannot contribute to the PL. Therefore, in combination with HEBM and selective-etching, additional strategies, such as an optimized electrochemical etching condition which has shown the potential to produce SiQD-only NPs,[39] will be adapted to further reducing the Si cores and hence increasing the PLQY of the SiQD-NPs.

In practice, the coverage of the silicon carbide (Si−C) bonds resulting from the photochemical hydrosilylation reaction can only reach up to 50% of the original silicon hydride (Si−H) sites due to the steric effect of UDA.[40] Therefore, part of the SiQD surfaces were still passivated with oxide-related chemistry, such as Si−O−Si and O−SiH, which is confirmed by the IR spectra in Figure 3. For the surface-oxidized SiQDs, the PL process is initiated by photoexcitation of charge carriers within the nanocrystals, followed by fast (τ in picoseconds) relaxation to the Si/SiO$_2$ interface.[41] Subsequently, almost all of the radiative recombination happens between groups of the
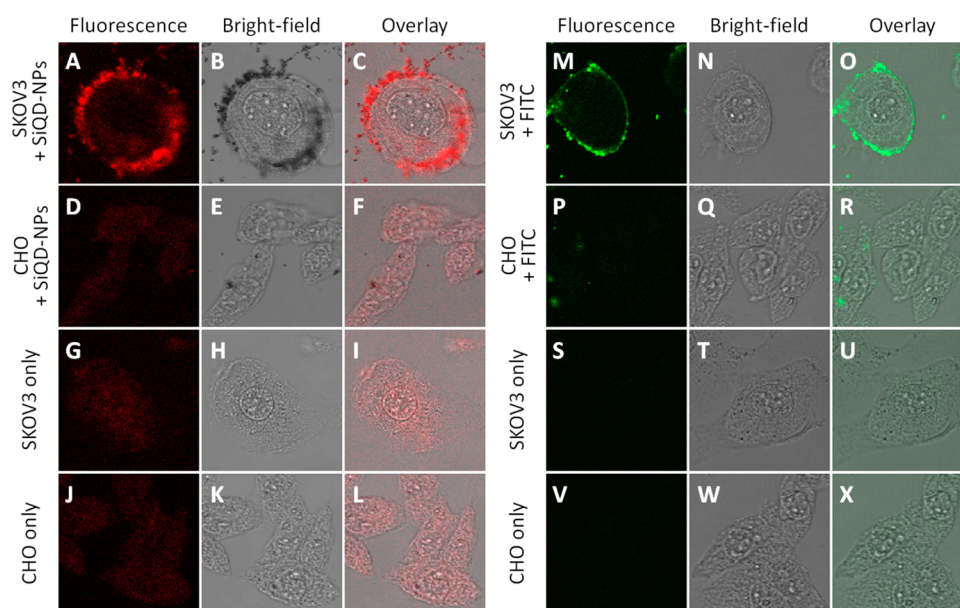
Figure 5. (A−C) SKOV3 cells and (D−F) CHO cells treated with the anti-HER2 conjugated SiQD-NPs under 405 nm excitation. (G−I) SKOV3 cells only and (J−L) CHO cells only under 405 nm excitation. (M−O) SKOV3 cells and (P−R) CHO cells treated with the FITC-modified anti-HER2 under 488 nm excitation. (S−U) SKOV3 cells only and (V−X) CHO cells only under 488 nm excitation. The physical dimension of each image is 62.53 μm × 62.53 μm. The image acquisition and processing settings are the same for A−L and M−X, respectively.

oxide-related defect states, while PL due to direct transitions between conduction band and valence band is negligible.[41] One characteristic of defect-mediated PL is the long lifetime, such as the microsecond-range PL lifetimes of the thiol- and BSA-terminated SiQD-NPs here (Figure 4F, G). On the contrary, organic dyes, such as fluorescein isothiocyanate (FITC), usually have much shorter PL lifetimes in nanoseconds (Figure 4E).

2.5. Immunostaining on Live Cancer Cells Using the Antibody-Conjugated SiQD-NPs. The confocal fluorescent images of live SKOV3 and CHO cells treated with the antibody-conjugated SiQD-NPs are shown on the left side of Figure 5. First, one end of the bifunctional polymer, isothiocyanate−PEG−isothiocyanate, was attached to the surface-immobilized BSA through isothiocyanate-amine coupling, leaving the other end available for conjugating to the antibodies. In this work, a clinical anti-HER2 monoclonal antibody, Trastuzumab, was used for immunostaining of the HER2-overexpressing SKOV3 cells. The HER2-nonexpressing CHO cells were used as control to evaluate the level of nonspecific binding. For preparing the anti-HER2 conjugated SiQD-NPs, the PEG-modified SiQD-NPs (0.51 mg mL^{-1}) were mixed with the anti-HER2 (0.13 mg mL^{-1}) in 0.1 M pH 6 PB for 3 h, followed by adding glycine to block the unreacted isothiocyanates and removing excess antibodies. Then, the live SKOV3 and CHO cells which had been previously seeded in different wells of a chamber slide were incubated at 37 °C and 5% CO_2 with the anti-HER2 conjugated SiQD-NPs (0.26 mg mL^{-1}) dispersed in the PB for 3 h. Subsequently, each well was gently washed by the PB two times, refilled with the PB, and put under a confocal fluorescent microscope for imaging, during which the focal plane was always positioned within the cytoplasm part. As expected, under 405 nm excitation, only the SKOV3 cells had the red-fluorescing SiQD-NPs binding to their membranes, whereas almost no nonspecific binding to the CHO cells was observed. Furthermore, the autofluorescence was low for both the SKOV3 and CHO cells only. In addition to one single cell (Figure 5A−C), multiple SKOV3 cells in a

group were also imaged, showing similar results (Figure S3). For comparison, the same batch of live SKOV3 and CHO cells were also incubated with the FITC-modified anti-HER2 (16.3 μg mL^{-1}) dispersed in the PB, as shown on the right side of Figure 5. Here the sample preparation and image acquisition steps were kept the same, except the excitation wavelength was changed to 488 nm. Likewise, the FITC-modified anti-HER2 successfully stained the SKOV3 cells. However, minor nonspecific binding to the CHO cells, as evidenced by the small bright spots in Figure 5R, was observed, likely because some anti-HER2 got agglomerated when mixing with FITC. Generally, the nonspecific binding became aggravated as the agglomerate size increased. In summary, the anti-HER2-conjugated SiQD-NPs showed obvious specific binding to the HER2-overexpressing SKOV3 cells and negligible nonspecific binding to the HER2-nonexpressing CHO cells. Furthermore, the immunofluorescence images obtained with the SiQD-NPs were close to those using FITC.

To further verify the specificity of the antibody-conjugated SiQD-NPs, we performed flow cytometry analysis on the cells used for the previous confocal study, as shown in Figure 6. The emission bandpass filter was at 615 nm for the SiQD-NPs and 525 nm for FITC. The excitation wavelength for all analysis here was 488 nm. The cell count profile of the HER2-overexpressing SKOV3 cells treated with the anti-HER2 conjugated SiQD-NPs (the green dash line in Figure 6A) was obviously shifted toward larger fluorescence intensity compared to the SKOV3 cells only (the purple solid line in Figure 6A), suggesting the red-fluorescing SiQD-NPs were attached to the SKOV3 cell membranes through the antibody−antigen specific binding. The same analysis was also conducted on the HER2-nonexpressing CHO cells. On the contrary, the CHO cell count profile after treated with the anti-HER2 conjugated SiQD-NPs (the green dash line in Figure 6B) was almost overlapped with its autofluorescence (the purple solid line in Figure 6B), indicating negligible nonspecific binding. For comparison, the cell count profiles of both the SKOV3 and CHO cells treated
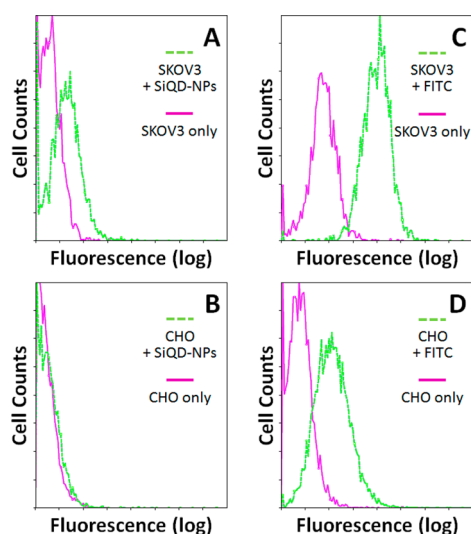
Figure 6. (A, B) Flow cytometry analysis on the SKOV3 and CHO cells that were treated (the green dash lines) and not treated (the purple solid lines) with the anti-HER2 conjugated SiQD-NPs, respectively. (C, D) Flow cytometry analysis on the SKOV3 and CHO cells treated (the green dash lines) and not treated (the purple solid lines) with the FITC-modified anti-HER2, respectively. The emission bandpass filter was at 615 nm for the SiQD-NPs and 525 nm for FITC. The excitation wavelength for all measurements here was 488 nm.

(the green dash lines in Figure 6C, D) and not treated (the purple solid lines in Figure 6C, D) with the FITC-modified anti-HER2 are shown. In contrast to the SiQD-NPs' result (Figure 6B), the FITC showed stronger nonspecific binding to the CHO cells (Figure 6D), which is in good accordance with the confocal imaging result (Figure 5R). Besides, the amount of peak shift resulting from the FITC (Figure 6C) was larger than the amount of peak shift resulting from the SiQD-NPs (Figure 6A), because the 488 nm excitation light, although ideal for FITC, cannot efficiently excite the SiQD-NPs, as indicated by their excitation spectrum (Figure 4D).

The in vitro photochemical stability of the antibody-conjugated SiQD-NPs was characterized and compared with FITC (Figure S4). The same SKOV3 cell immunostained by either the SiQD-NPs or FITC was consecutively scanned by the confocal microscope multiple times, with each scanning process extended to about 3 min. The PL intensity after each time of scanning was qualitatively and quantitatively analyzed. After five times of scanning, the peak PL intensity of the SiQD-NPs decreased to a plateau at about 50% of the original value. In comparison, the peak PL intensity of FITC dropped about 60% with a trend of persistent monotonic decreasing. The photobleaching of FITC has been known to be associated with the structural damage of its conjugated double bond system. On the other hand, the initial fast PL decay of the SiQD-NPs can be mainly attributed to emission intermittency, i.e., the blinking effect.[42] Under high intensity excitation by the focused 405 nm laser beam of the confocal microscope, the SiQDs with such a long PL lifetime (Figure 4G) might easily enter the multiexciton regime, in which inelastic exciton−exciton scattering could create charge separation. Once in the charge-separated state, the Auger recombination efficiently quenched all the excitons photoexcited thereafter and hence stopped the SiQD from emitting PL until the separated charges were neutralized.[42] Experimentally, when the excitation source was

removed, partial PL recovery of the SiQD-NPs has been observed, indicating that some dark SiQDs were capable of going back to their single-exciton mode. Furthermore, at relatively low excitation intensity, the SiQD-NPs showed almost no PL degradation under continuous illumination for up to 20 h (Figure S5). Therefore, in practical applications, keeping the excitation intensity low while further improving the PLQY is critical to avoid the blinking effect of the SiQD-NPs with microsecond-range PL lifetimes.

The in vitro cell viability assay for the BSA-terminated SiQD-NPs to the SKOV3 cell line after 24 and 48 h of treatment was conducted (Figure 7). For the 24 h treatment, the BSA-
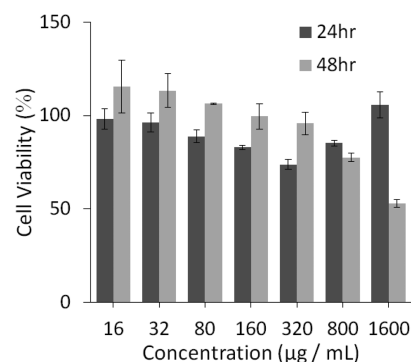

Figure 7. Cell viability of the SKOV3 cells after treatment of the BSA-terminated SiQD-NPs of varying concentrations for 24 and 48 h.

terminated SiQD-NPs showed minimal cytotoxicity at concentration up to 1600 μg mL^{-1} in the medium, which is much higher than the concentration (260 μg mL^{-1}) used for the confocal fluorescent imaging in Figure 5. Interestingly, at concentrations higher than 320 μg mL^{-1}, the cell viability moderately increased, likely because the BSA coating might provide additional nutrition to the SKOV3 cells during treatment, given that BSA is a major component of fetal bovine serum (FBS), which is a widely used serum-based supplement for in vitro cell culture. For the 48 h treatment, the IC$_{50}$ of the BSA-terminated SiQD-NPs was determined to be about 1600 μg mL^{-1}, which is about 3 times higher than the IC$_{50}$ of other biocompatible SiQDs encapsulated in phospho-lipid micelles.[17]

3. CONCLUSION

In conclusion, we synthesized water-dispersible and highly photoluminescent SiQD-NPs as biocompatible biological labels with antifouling coatings composed of BSA and PEG, and their outmost surfaces were terminated with isothiocyanates for facile and consistent conjugation to the antibodies. The relatively monodisperse SiQD-NPs of diameter about 130 nm were synthesized by a novel top-down method, including electro-chemical etching to produce a porous silicon layer, photo-chemical hydrosilylation on the SiQDs, high energy ball milling, and "selective-etching" in HNO$_3$ and HF to remove the nonradiative microsize Si cores. Then, the organic capping elements, including BSA, PEG, and the antibodies, were sequentially grafted to the SiQD-NP surface through different presynthesized chemical linkers that can form stable covalent bonding by either maleimide−thiol or isothiocyanate-amine coupling. Under near-UV excitation, the SiQD-NP suspension in THF emitted bright reddish PL (peak at 621 nm and fwhm = 114 nm) with PLQY = 45 to 55%, which however was

quenched to 5 to 10% after the suspension medium was changed to the PB. The decrease of PLQY was likely associated with the absorption of polar molecules on the SiQD surfaces which enhanced nonradiative recombination processes. For the photochemical stability of the SiQD-NPs, the initial fast PL decay under high intensity excitation can be mainly attributed to the blinking effect of the SiQDs with microsecond-range PL lifetimes. The in vitro cell viability assay revealed that the BSA-terminated SiQD-NPs had exceptional biocompatibility, with IC_{50} = about 1600 μg mL^{-1} after 48 h of treatment. Finally, through confocal fluorescent imaging and flow cytometry analysis, the anti-HER2 conjugated SiQD-NPs showed obvious specific binding to the HER2-overexpressing SKOV3 cells and negligible nonspecific binding to the HER2-nonexpressing CHO cells. Under similar experimental conditions, the immunofluorescence results obtained with the SiQD-NPs were close to those using conventional organic dyes, such as FITC.

4. EXPERIMENTAL SECTION

Materials. N-(2-Aminoethyl)maleimide trifluoroacetate salt, 1,1′-Thiocarbonyldi-2(1H)-pyidone, 2,2′-(Ethylenedioxy)diethanethiol (EDDT), methyl chloroformate, fluorescein isothiocyanate (FITC) and quinine sulfate were purchased from Sigma-Aldrich. 10-Undecen-1-ol (UDA), p-Toluenesulfonyl chloride (TsCl), and $H_2N-PEG-NH_2$ were purchased from Alfa Aesar. Triethylamine (NEt_3) was purchased from Merck, carbon disulfide (CS_2) from Kanto Chemicals and BSA (biotechnology grade) from Amresco. All reagents were used as received without further purification. Deionized water (18.2 MΩ) produced by Milli-Q water purification system was used for preparing all aqueous buffers and solutions. Anti-HER2 were extracted and purified from Herceptin Trastuzumab using spin column (MWCO = 3K). FITC-modified anti-HER2 were prepared by mixing FITC (0.16 mg mL^{-1}) and anti-HER2 (2 mg mL^{-1}) in 0.1 M pH 7 phosphate-buffered saline, followed by passing through desalting column and concentrating with spin column. SKOV3 and CHO cell lines were obtained from Industrial Technology Research Institute, and cultured in BI RPMI 1640 added with L-Glutamine, 10% FBS and some antibiotics at 37 °C and 5% CO_2. The chamber slide used for the seeding of both SKOV3 and CHO cells was μ-slide 8 well ibiTreat from Ibidi.

Synthesis of 1-(2-Isothiocyanatoethyl)-1H-pyrrole-2,5-dione (MaNCS). In a 250 mL round-bottomed flask, N-(2-aminoethyl)-maleimide trifluoroacetate salt (0.82 g, 3.27 mmol) was suspended in 20 mL of anhydrous CH_2Cl_2 under a N_2 atmosphere. NEt_3 (0.13 mL, 0.98 mmol) and 1,1′-Thiocarbonyldi-2(1H)-pyidone (0.81 g, 3.43 mmol) were added into the flask, and the mixture was stirred for 4 h at room temperature. The progress of the reaction was monitored by TLC. Flash chromatography of the residue (MeOH: CH_2Cl_2 = 1:20) yielded the desired product as white powder (0.45 g, 74%). R_f = 0.4 (Silica gel, MeOH: CH_2Cl_2 = 1:15); IR (ATR, cm^{-1}) 3150, 2100, 1700, 1450, 830. ^1H NMR (300 MHz, $CDCl_3$) δ 6.77 (s, 2H, 2 × CH), 3.85–3.77 (m, 2H, CH_2), 3.77–3.69 (m, 2H, CH_2). ^{13}C NMR (75.4 MHz, $CDCl_3$) δ 170.0 (2× s), 134.3 (2× d + s), 43.3 (t), 37.0 (t). M.S. (EI) cal'd for $C_7H_6N_2O_2S$ 182.0, found 182.0. The full ^1H NMR, ^{13}C NMR, ATR-FTIR, and EI-MS spectra of MaNCS are shown in Figures S6–S9, respectively.

Synthesis of Isothiocyanate–PEG–Isothiocyanate. In a 50 mL round-bottomed flask, $H_2N-PEG-NH_2$ (M_w = 3350, 0.5 g, 0.17 mmol) was dissolved in 4 mL of anhydrous $CHCl_3$ under a N_2 atmosphere. To this solution was added NEt_3 (60 μL, 0.43 mmol) and then CS_2 (26 μL, 0.43 mmol). The reaction mixture was stirred for 2 h at room temperature before cooling to 0 °C and adding methyl chloroformate (36 μL, 0.43 mmol). After 30 min, the reaction mixture was stirred for another 2 h at room temperature. Then the solvent and excess reagents were removed by rotary evaporator and vacuum pump. The product was further purified by flash chromatography (MeOH: CH_2Cl_2 = 1:10, 0.4 g, 67%). R_f = 0.4 (silica gel, MeOH: CH_2Cl_2 = 1:15); IR (ATR, cm^{-1}) 2900, 1480, 1100, 970, 820. ^1H NMR (300 MHz, $CDCl_3$) δ 3.95–3.80 (m, CH_2, 5H), 3.72–3.55 (m, CH_2, 300H), 3.40–3.30 (m, CH_2, 2H). To verify the amine terminations were successfully converted to the isothiocyanate terminations, we compared the ^1H NMR and ATR-FTIR spectra of both $H_2N-PEG-NH_2$ and isothiocyanate–PEG–isothiocyanate side by side, as shown in Figures S10–S13.

Synthesis of the Hydroxyl-Terminated SiQD-NPs. The key fabrication steps in Figure 1 are described in detail as following. A 6-in. p-type silicon wafer from Silicon Inc. with orientation (100) and resistivity 5−10 ohm-cm was electrochemically etched at a constant current density = 2.80 mA cm^{-1} in an electrolyte mixture comprising 49% HF:MeOH = 13:22 (volume ratio) for 1 h. After treated with diluted HF, the silicon wafer was immediately immersed in deoxygenated neat UDA inside a nitrogen-filled chamber, followed by illumination under a 24 W white light LED lamp at room temperature for 6 h for the photochemical hydrosilylation reaction. The porous silicon layer on top of the silicon wafer surface was mechanically pulverized to produce silicon powders of about 50 mg per wafer. The silicon powders were dispersed in isopropanol for HEBM by Retsch Emax with 3 mm zirconia beads for 20 h. The silicon powders were selectively etched by an aqueous etchant comprising 49% HF: 70% HNO_3 = 1:40 (volume ratio) for about 5−10 min and then washed by copious amount of deionized water. The resulting hydroxyl-terminated SiQD-NPs, about 25 mg per wafer, looked like yellowish fine powders under room light and exhibited bright reddish PL under 365 nm excitation.

Synthesis of the BSA-Terminated SiQD-NPs. In a 50 mL round-bottomed flask, the hydroxyl-terminated SiQD-NPs (about 10 mg) were sonicated with TsCl (1.00 g, 5.25 mmol) in 15 mL anhydrous ethyl acetate under a N_2 atmosphere for 6 h. Immediately afterward, in another 50 mL round-bottomed flask, the resulting OTs-terminated SiQD-NPs were stirred with EDDT (1 mL, 5.84 mmol) in 15 mL anhydrous ethyl acetate for another 12 h. Next, the resulting thiol-terminated SiQD-NPs (about 3 mg mL^{-1}) were vortexed with MaNCS (0.05 M) in dimethyl sulfoxide for 12 h. Finally, the resulting isothiocyanate-terminated SiQD-NPs (about 3 mg mL^{-1}) were vortexed with BSA (5 mg mL^{-1}) in 0.1 M pH 6 PB at 4 °C for 12 h. The resulting BSA-terminated SiQD-NPs were uniformly dispersed in 0.1 M pH 6 PB, and stored at 4 °C for the following bioconjugation to the antibodies.

Synthesis of the Anti-HER2 Conjugated SiQD-NPs. The BSA-terminated SiQD-NPs (0.51 mg mL^{-1}) were vortexed with the isothiocyanate–PEG–isothiocyanate (0.01 M) in 0.1 M pH 6 PB at room temperature for 3 h. Subsequently, the PEG-modified SiQD-NPs (0.51 mg mL^{-1}) were mildly vortexed with anti-HER2 (0.13 mg mL^{-1}) in 0.1 M pH 6 PB at room temperature for 3 h, followed by adding glycine (0.1 M) to block the unreacted isothiocyanates and washing with copious amount of the PB to remove excess antibodies. The resulting anti-HER2 conjugated SiQD-NPs had appearance close to the BSA-terminated ones, and were stored at 4 °C not more than 12 h prior to the immunofluorescence studies here. However, experimentally we also found that the stock anti-HER2 conjugated SiQD-NPs had the same performance as freshly prepared ones after being stored at 4 °C for several weeks.

In Vitro Cell Viability Assay for the BSA-Terminated SiQD-NPs. The in vitro cytotoxicity of the BSA-terminated SiQD-NPs was assayed with an MTT cell viability kit (AppliChem). MTT (3-(4,5-Dimethylthiazol-2-yl)-2,5-diphenyltetrazolium bromide) powder was dissolved in 1× DPBS (Dulbecco's phosphate-buffered saline), and the resulting solution (5 mg mL^{-1}) was filtered through a 0.22 μm sterilized syringe filter and stored at 4 °C. The SKOV3 cells were seeded in a 96-well culture plate, with each well containing 5 × 10^3 cells in 100 μL RPMI medium, and incubated at 37 °C and 5% CO_2 for 24 h. Then, the medium was replaced by 100 μL fresh medium containing the BSA-terminated SiQD-NPs of varying concentrations. After 24- or 48-h incubation, each well was washed two times with fresh medium and added with diluted MTT solution (1 mg mL^{-1}). After 4 h of incubation, the MTT solution was withdrawn and 100 μL DMSO was added to each well. The plate was gently swirled at room

temperature for 15 min. Finally, using an ELISA microplate reader, the cell viability (%) was determined by the absorbance at 570 nm of each well treated with the BSA-terminated SiQD-NPs relative to the control well, which contained the SKOV3 cells only. A complete assay was performed thrice, and results were averaged.

Characterization. HRTEM images were recorded with a JEOL ARM200F spherical aberration corrected scanning transmission electron microscope. SEM images were recorded with a JEOL JSM-7401F scanning electron microscope. DLS particle size distributions of the SiQD-NPs were obtained by a Brookhaven BI-200SM particle size analyzer, with NNLS rms error $<1.5 \times 10^{-3}$, sample size $>1.2 \times 10^8$, data retention rate >95% and agglomeration percentage <5%. Particle size distributions of the microsize Si particles were obtained by a Horiba Partica LA-950 V2 laser scattering particle size distribution analyzer. ATR-FTIR spectra were collected on a Shimadzu IRTracer-100 equipped with MIRacle-10. All IR samples were in dried powder forms with solvents fully evaporated. Photoluminescence and excitation spectra were collected on a Jobin Yvon Horiba FluoroMax-3, absorbance spectra on a Hitachi U-3010 spectrophotometer and PL lifetimes on an Edinburgh FS5 spectrofluorometer. PLQYs were measured using a Jobin Yvon Horiba Fluorolog-3 equipped with an integrating sphere. The optical system was calibrated by a standard dye sample, quinine sulfate in 0.1 M H_2SO_4, which has PLQY = 54%. Confocal fluorescent images were recorded with a Leica TSC SP5 II and a water immersion objective with numerical aperture =1.2. The emission collection window was 600−700 nm and 500−550 nm for the SiQD-NPs and FITC, respectively. With one excitation wavelength, either 405 or 488 nm, all images were acquired and processed using identical settings. Flow cytometry analysis was performed on a Beckman Coulter Cytomics FC500. The total counts of the SKOV3 cells only, treated with the anti-HER2 conjugated SiQD-NPs and treated with the FITC-modified anti-HER2 were equal to 3055, 2135 and 2812, respectively. On the other hand, the total counts of the CHO cells only, treated with the anti-HER2 conjugated SiQD-NPs and treated with the FITC-modified anti-HER2 were equal to 10000, 7971 and 7547, respectively.

ASSOCIATED CONTENT

Supporting Information

The Supporting Information is available free of charge on the ACS Publications website at DOI: 10.1021/acsami.6b02318.

Photographs of the 6 in. silicon wafers after electrochemical etching and after photochemical hydrosilylation; SEM images of the porous silicon layer, the silicon powders collected after pulverization of the porous silicon layer, and the SiQD-NPs after HEBM and selective-etching; confocal fluorescent images of multiple SKOV3 cells immunostained by the SiQD-NPs; in vitro and long-term photochemical stability of the SiQD-NPs. ^1H NMR, ^{13}C NMR, ATR-FTIR, and EI-MS spectra of MaNCS. Side-by-side comparison of ^1H NMR and ATR-FTIR spectra of $H_2N-PEG-NH_2$ and isothiocyanate−PEG−isothiocyanate (PDF)

AUTHOR INFORMATION

Corresponding Author
*E-mail: ykl@faculty.nctu.edu.tw. Tel: +886 3 5712121 ext. 56545.

Notes
The authors declare no competing financial interest.

REFERENCES

(1) Stephens, D. J.; Allan, V. J. Light Microscopy Techniques for Live Cell Imaging. *Science* **2003**, *300*, 82−86.
(2) Michalet, X.; Pinaud, F. F.; Bentolila, L. A.; Tsay, J. M.; Doose, S.; Li, J. J.; Sundaresan, G.; Wu, A. M.; Gambhir, S. S.; Weiss, S. Quantum Dots for Live Cells, In Vivo Imaging, and Diagnostics. *Science* **2005**, *307*, 538−544.
(3) Medintz, I. L.; Uyeda, H. T.; Goldman, E. R.; Mattoussi, H. Quantum Dot Bioconjugates for Imaging, Labelling and Sensing. *Nat. Mater.* **2005**, *4*, 435−446.
(4) Veiseh, M.; Gabikian, P.; Bahrami, S.-B.; Veiseh, O.; Zhang, M.; Hackman, R. C.; Ravanpay, A. C.; Stroud, M. R.; Kusuma, Y.; Hansen, S. J.; Kwok, D.; Munoz, N. M.; Sze, R. W.; Grady, W. M.; Greenberg, N. M.; Ellenbogen, R. G.; Olson, J. M. Tumor Paint: A Chlorotoxin:Cy5.5 Bioconjugate for Intraoperative Visualization of Cancer Foci. *Cancer Res.* **2007**, *67*, 6882−6888.
(5) Song, L.; Hennink, E. J.; Young, I. T.; Tanke, H. J. Photobleaching Kinetics of Fluorescein in Quantitative Fluorescence Microscopy. *Biophys. J.* **1995**, *68*, 2588−2600.
(6) Resch-Genger, U.; Grabolle, M.; Cavaliere-Jaricot, S.; Nitschke, R.; Nann, T. Quantum Dots versus Organic Dyes as Fluorescent Labels. *Nat. Methods* **2008**, *5*, 763−775.
(7) Bruchez, M., Jr.; Moronne, M.; Gin, P.; Weiss, S.; Alivisatos, A. P. Semiconductor Nanocrystals as Fluorescent Biological Labels. *Science* **1998**, *281*, 2013−2016.
(8) Jaiswal, J. K.; Mattoussi, H.; Mauro, J. M.; Simon, S. M. Long-term Multiple Color Imaging of Live Cells Using Quantum Dot Bioconjugates. *Nat. Biotechnol.* **2002**, *21*, 47−51.
(9) Dubertret, B.; Skourides, P.; Norris, D. J.; Noireaux, V.; Brivanlou, A. H.; Libchaber, A. In Vivo Imaging of Quantum Dots Encapsulated in Phospholipid Micelles. *Science* **2002**, *298*, 1759−1762.
(10) Gao, X.; Cui, Y.; Levenson, R. M.; Chung, L. W. K.; Nie, S. In Vivo Cancer Targeting and Imaging with Semiconductor Quantum Dots. *Nat. Biotechnol.* **2004**, *22*, 969−976.
(11) Zimmer, J. P.; Kim, S. W.; Ohnishi, S.; Tanaka, E.; Frangioni, J. V.; Bawendi, M. G. Size Series of Small Indium Arsenide−Zinc Selenide Core−Shell Nanocrystals and Their Application to In Vivo Imaging. *J. Am. Chem. Soc.* **2006**, *128*, 2526−2527.
(12) Pons, T.; Pic, E.; Lequeux, N.; Cassette, E.; Bezdetnaya, L.; Guillemin, F.; Marchal, F.; Dubertret, B. Cadmium-Free CuInS$_2$/ZnS Quantum Dots for Sentinel Lymph Node Imaging with Reduced Toxicity. *ACS Nano* **2010**, *4*, 2531−2538.
(13) Ye, L.; Yong, K.-T.; Liu, L.; Roy, I.; Hu, R.; Zhu, J.; Cai, H.; Law, W.-C.; Liu, J.; Wang, K.; Liu, J.; Liu, Y.; Hu, Y.; Zhang, X.; Swihart, M. T.; Prasad, P. N. A Pilot Study in Non-Human Primates Shows No Adverse Response to Intravenous Injection of Quantum Dots. *Nat. Nanotechnol.* **2012**, *7*, 453−458.
(14) He, Y.; Zhong, Y.; Peng, F.; Wei, X.; Su, Y.; Lu, Y.; Su, S.; Gu, W.; Liao, L.; Lee, S.-T. One-Pot Microwave Synthesis of Water-Dispersible, Ultraphoto- and pH-Stable, and Highly Fluorescent Silicon Quantum Dots. *J. Am. Chem. Soc.* **2011**, *133*, 14192−14195.
(15) Zhong, Y.; Peng, F.; Bao, F.; Wang, S.; Ji, X.; Yang, L.; Su, Y.; Lee, S.-T.; He, Y. Large-Scale Aqueous Synthesis of Fluorescent and Biocompatible Silicon Nanoparticles and Their Use as Highly Photostable Biological Probes. *J. Am. Chem. Soc.* **2013**, *135*, 8350−8356.
(16) Zhong, Y.; Peng, F.; Wei, X.; Zhou, Y.; Wang, J.; Jiang, X.; Su, Y.; Su, S.; Lee, S.-T.; He, Y. Microwave-Assisted Synthesis of Biofunctional and Fluorescent Silicon Nanoparticles Using Proteins as Hydrophilic Ligands. *Angew. Chem., Int. Ed.* **2012**, *51*, 8485−8489.

(17) Erogbogbo, F.; Yong, K.-T.; Roy, I.; Hu, R.; Law, W.-C.; Zhao, W.; Ding, H.; Wu, F.; Kumar, R.; Swihart, M. T.; Prasad, P. N. In Vivo Targeted Cancer Imaging, Sentinel Lymph Node Mapping and Multi-Channel Imaging with Biocompatible Silicon Nanocrystals. *ACS Nano* **2011**, *5*, 413−423.

(18) Park, J.-H.; Gu, L.; von Maltzahn, G.; Ruoslahti, E.; Bhatia, S. N.; Sailor, M. J. Biodegradable Luminescent Porous Silicon Nanoparticles for In Vivo Applications. *Nat. Mater.* **2009**, *8*, 331−336.

(19) Chinnathambi, S.; Chen, S.; Ganesan, S.; Hanagata, N. Silicon Quantum Dots for Biological Applications. *Adv. Healthcare Mater.* **2014**, *3*, 10−29.

(20) Erogbogbo, F.; Yong, K.-T.; Roy, I.; Xu, G.; Prasad, P. N.; Swihart, M. T. Biocompatible Luminescent Silicon Quantum Dots for Imaging of Cancer Cells. *ACS Nano* **2008**, *2*, 873−878.

(21) Canham, L. T. Silicon Quantum Wire Array Fabrication by Electrochemical and Chemical Dissolution of Wafers. *Appl. Phys. Lett.* **1990**, *57*, 1046−1048.

(22) Li, X.; He, Y.; Talukdar, S. S.; Swihart, M. T. Process for Preparing Macroscopic Quantities of Brightly Photoluminescent Silicon Nanoparticles with Emission Spanning the Visible Spectrum. *Langmuir* **2003**, *19*, 8490−8496.

(23) Mangolini, L.; Thimsen, E.; Kortshagen, U. High-Yield Plasma Synthesis of Luminescent Silicon Nanocrystals. *Nano Lett.* **2005**, *5*, 655−659.

(24) Holmes, J. D.; Ziegler, K. J.; Doty, R. C.; Pell, L. E.; Johnston, K. P.; Korgel, B. A. Highly Luminescent Silicon Nanocrystals with Discrete Optical Transitions. *J. Am. Chem. Soc.* **2001**, *123*, 3743−3748.

(25) Henderson, E. J.; Kelly, J. A.; Veinot, J. G. C. Influence of $HSiO_{1.5}$ Sol−Gel Polymer Structure and Composition on the Size and Luminescent Properties of Silicon Nanocrystals. *Chem. Mater.* **2009**, *21*, 5426−5434.

(26) Baldwin, R. K.; Pettigrew, K. A.; Garno, J. C.; Power, P. P.; Liu, G.-y.; Kauzlarich, S. M. Room Temperature Solution Synthesis of Alkyl-Capped Tetrahedral Shaped Silicon Nanocrystals. *J. Am. Chem. Soc.* **2002**, *124*, 1150−1151.

(27) Choi, H. S.; Liu, W.; Misra, P.; Tanaka, E.; Zimmer, J. P.; Ipe, B. I.; Bawendi, M. G.; Frangioni, J. V. Renal Clearance of Quantum Dots. *Nat. Biotechnol.* **2007**, *25*, 1165−1170.

(28) Nel, A.; Xia, T.; Madler, L.; Li, N. Toxic Potential of Materials at the Nanolevel. *Science* **2006**, *311*, 622−627.

(29) Tu, C.-C.; Chou, Y.-N.; Hung, H.-C.; Wu, J.; Jiang, S.; Lin, L. Y. Fluorescent Porous Silicon Biological Probes with High Quantum Efficiency and Stability. *Opt. Express* **2014**, *22*, 29996−30003.

(30) Stewart, M. P.; Buriak, J. M. Exciton-Mediated Hydrosilylation on Photoluminescent Nanocrystalline Silicon. *J. Am. Chem. Soc.* **2001**, *123*, 7821−7830.

(31) Cullis, A. G.; Canham, L. T. Visible Light Emission Due to Quantum Size Effects in Highly Porous Crystalline Silicon. *Nature* **1991**, *353*, 335−338.

(32) Wright, A. K.; Thompson, M. R. Hydrodynamic Structure of Bovine Serum Albumin Determined by Transient Electric Birefringence. *Biophys. J.* **1975**, *15*, 137−141.

(33) Tan, Y. H.; Liu, M.; Nolting, B.; Go, J. G.; Gervay-Hague, J.; Liu, G.-y A Nanoengineering Approach for Investigation and Regulation of Protein Immobilization. *ACS Nano* **2008**, *2*, 2374−2384.

(34) Linegar, K. L.; Adeniran, A. E.; Kostko, A. F.; Anisimov, M. A. Hydrodynamic Radius of Polyethylene Glycol in Solution Obtained by Dynamic Light Scattering. *Colloid J.* **2010**, *72*, 279−281.

(35) Moore, J. M. R.; Patapoff, T. W.; Cromwell, M. E. M. Kinetics and Thermodynamics of Dimer Formation and Dissociation for a Recombinant Humanized Monoclonal Antibody to Vascular Endothelial Growth Factor. *Biochemistry* **1999**, *38*, 13960−13967.

(36) Kůsová, K.; Cibulka, O.; Dohnalová, K.; Pelant, I.; Valenta, J.; Fučíková, A.; Žídek, K.; Lang, J.; Englich, J.; Matějka, P.; Štěpánek, P.; Bakardjieva, S. Brightly Luminescent Organically Capped Silicon Nanocrystals Fabricated at Room Temperature and Atmospheric Pressure. *ACS Nano* **2010**, *4*, 4495−4504.

(37) Tu, C.-C.; Hoo, J.-H.; Böhringer, K. F.; Lin, L. Y.; Cao, G. Surface Passivation Dependent Photoluminescence from Silicon Quantum Dot Phosphors. *Opt. Lett.* **2012**, *37*, 4771−4773.

(38) Lauerhaas, J. M.; Sailor, M. J. Chemical Modification of the Photoluminescence Quenching of Porous Silicon. *Science* **1993**, *261*, 1567−1568.

(39) Wang, J.; Liu, Y.; Peng, F.; Chen, C.; He, Y.; Ma, H.; Cao, L.; Sun, S. A General Route to Efficient Functionalization of Silicon Quantum Dots for High-Performance Fluorescent Probes. *Small* **2012**, *8*, 2430−2435.

(40) Buriak, J. M. Organometallic Chemistry on Silicon and Germanium Surfaces. *Chem. Rev.* **2002**, *102*, 1271−1308.

(41) Dohnalová, K.; Kůsová, K.; Pelant, I. Time-Resolved Photoluminescence Spectroscopy of the Initial Oxidation Stage of Small Silicon Nanocrystals. *Appl. Phys. Lett.* **2009**, *94*, 211903.

(42) Valenta, J.; Fucikova, A.; Vácha, F.; Adamec, F.; Humpolíčková, J.; Hof, M.; Pelant, I.; Kůsová, K.; Dohnalová, K.; Linnros, J. Light-Emission Performance of Silicon Nanocrystals Deduced from Single Quantum Dot Spectroscopy. *Adv. Funct. Mater.* **2008**, *18*, 2666−2672.